

# HEAT TRANSFER EFFECTS ON A FULLY PREMIXED METHANE IMPINGING FLAME

**D. Mira<sup>1</sup>, M. Zavala<sup>1</sup>, M. Avila<sup>1</sup>, H. Owen<sup>1</sup>, J.C. Cajas<sup>1</sup>,  
G. Houzeaux<sup>1</sup> and M. Vazquez<sup>1</sup>**

<sup>1</sup> *Barcelona Supercomputing Center (BSC-CNS), Barcelona, Spain*  
[daniel.mira@bsc.es](mailto:daniel.mira@bsc.es)

## 1 Introduction

The effects of heat transfer on engineering applications is a fundamental aspect in the design of power and propulsive systems. The heat exchange between fluid and solid parts may reduce the efficiency of the system in situations where temperature peaks and gradients become important. This is the case of gas turbines, combustion engines or cooling of turbine blades. However, this interaction is difficult to model numerically not only due to the different time scales governing each individual problem, but also due to instability issues related to the coupling strategy (Bunker, 2007). The coupling of the Navier-Stokes equations with the heat equation, also referred as conjugate heat transfer, usually requires the existence of two different solvers, one for each domain, exchanging information at specified boundaries. Partitioned or staggered algorithms can be applied to control the exchange of information allowing the solvers to advance at different time-steps with the most suitable formulation for each physical problem (Farhat and Lesoinne, 2000).

An interesting application to evaluate the numerical algorithms and the effects of the thermal coupling with the flow dynamics is the case of a jet flame impinging on a flat plate. In this configuration, high rates of wall heat transfer are achieved as a consequence of the enhancement of the heat transfer coefficients by the continuous impact of vortical structures on the plate (Mira et al., 2013). Impinging jets are characterised by the nozzle-to-plate distance H/D and the dynamics of the flow is highly dependent on this ratio (Hadziabic and Hanjalic, 2008). Three flow regions can be identified in this configuration: the free jet region where flow is not influenced by the plate, the deflection region and the wall jet region. For large H/D ratios, the configuration permits the development of a free jet and the impingement leads to the formation of a heat transfer profile with a maximum located at the stagnation point. However, for small H/D ratios, the jet core may be longer than the H/D distance causing the jet to be laminar at the plate featuring low levels of turbulence and a minimum heat transfer coefficients at the stagnation point. As the flow accelerates parallel to the plate,

the wall shear stresses increase leading to a maximum in the heat transfer profile at the wall (Fuchs and Halqvist, 2009).

The aim of the present work is to investigate the heat transfer effects and flow dynamics of an impinging flame with low nozzle-to-plate distance when the solid plate is considered non-adiabatic and the heat flux through it is solved by the heat conduction equation.

## 2 Mathematical formulation

### Governing equations

The governing equations describing the reacting flow field correspond to the low Mach number approximation of the Navier-Stokes equations along with the species conservation equations in the context of large-eddy simulation (LES).

The flow field is filtered in space using a box filter given by  $\Delta = V^{1/3}$ , where  $V$  represents the cell volume and a Favre filter operator is employed to account for the density variations. The filtered governing equations for multi-species reacting flows read:

$$\frac{\partial \bar{\rho}}{\partial t} + \nabla \cdot (\bar{\rho} \tilde{\mathbf{u}}) = 0 \quad (1)$$

$$\bar{\rho} \frac{\partial \tilde{\mathbf{u}}}{\partial t} + \bar{\rho} \tilde{\mathbf{u}} \cdot \nabla \tilde{\mathbf{u}} - \nabla \cdot (\mu \boldsymbol{\tau}(\tilde{\mathbf{u}})) + \nabla \bar{p} = \bar{\rho} \mathbf{g} + \nabla \cdot \boldsymbol{\tau}^{sgs} \quad (2)$$

$$\begin{aligned} \bar{\rho} c_p \frac{\partial \tilde{T}}{\partial t} + \bar{\rho} c_p \tilde{\mathbf{u}} \cdot \nabla \tilde{T} - \nabla \cdot (k \nabla \tilde{T}) - \alpha \tilde{T} \frac{dp^{th}}{dt} = \\ - \sum_k \bar{h}_k \bar{\omega}_k - \sum_k \bar{\rho} c_{p,k} D_k \nabla \tilde{T} \cdot \nabla \tilde{Y}_k + \nabla \cdot h^{sgs} \end{aligned} \quad (3)$$

$$\begin{aligned} \bar{\rho} \frac{\partial \tilde{Y}_k}{\partial t} + \bar{\rho} \tilde{\mathbf{u}} \cdot \nabla \tilde{Y}_k - \nabla \cdot (\bar{\rho} D_k \nabla \tilde{Y}_k) = \bar{\omega}_k + \nabla \cdot \Phi_m^{sgs} \\ k = 1, \dots, N \end{aligned} \quad (4)$$

where  $\mu$  is the viscosity of the mixture,  $\boldsymbol{\tau}(\tilde{\mathbf{u}}) = \frac{1}{2}(\nabla \tilde{\mathbf{u}} + \nabla^T \tilde{\mathbf{u}}) - \frac{1}{3} \nabla \cdot \tilde{\mathbf{u}} \mathbf{I}$  is the deviatoric part of the rate of deformation tensor and  $\mathbf{I}$  the identity tensor.  $p^{th}$  is the thermodynamic pressure, which for the open flow case is set to constant and equal to the external pressure.  $\alpha$  is the thermal expansion coefficient, usually  $\alpha \simeq 1/\tilde{T}$  (Avila et al., 2011),  $k$  is the thermal conductivity of the mixture, and  $\bar{h}_k$  and  $c_{p,k}$  are the

enthalpy and the specific heat of each species  $k$ . The production rate of the  $k$ th species  $\dot{\omega}_k$  is obtained as a summation of all reactions involving species  $k$  and as only one chemical reaction is included, the production rate equals the rate of progress  $\dot{\omega}_k = \dot{\omega}$ . The index  $m = (1 \text{ to } N)$  denotes the individual species, while the superscript  $sgs$  refers to the subgrid scale terms coming from the filtering operation.

The variables with superscript  $sgs$  correspond to the unresolved momentum transport  $\tau^{sgs} = \bar{\rho}(\tilde{\mathbf{u}}\tilde{\mathbf{u}} - \tilde{\mathbf{u}}\tilde{\mathbf{u}})$ , the unresolved heat flux  $h^{sgs} = \bar{\rho}(\tilde{\mathbf{u}}T - \tilde{\mathbf{u}}\tilde{T})$  and the unresolved species mass flux  $\Phi_k^{sgs} = \bar{\rho}(\tilde{\mathbf{u}}\tilde{Y}_k - \tilde{\mathbf{u}}\tilde{Y}_k)$  respectively. The subgrid scale momentum transport is modelled using an eddy viscosity  $\nu_t$  obtained by the Wall-Adapting Local Eddy-viscosity (WALE) model proposed by Nicoud and Ducros (1999). The heat flux in the subgrid scale  $h^{sgs}$  as well as the subgrid scale species mass flux  $\Phi_k^{sgs}$  are both modelled using a gradient diffusion approach (Mira et al., 2013). The solid part of the domain will be treated by the conjugate heat transfer (CHT) approach for which the heat equation is solved.

$$\bar{\rho}c_p \frac{\partial T}{\partial t} = \nabla \cdot (k \nabla T) + q \quad (5)$$

### Coupling approach for the LES-CHT simulation

The coupling of the conjugate heat transfer of the solid domain with the LES solver is accomplished in such a way that the fluid imposes the heat flux to the CHT solver, while the solid imposes the skin temperature  $T_s$  to the fluid. The boundary conditions are imposed over the interface using the nature of the information received by each solver. The heat equation requires a Neumann-type boundary condition  $q = q_s$ , while the Low-Mach fluid uses a Dirichlet-type boundary condition for the temperature  $T = T_s$  (Jaiman et al., 2006). The coupling of the solid and fluid meshes is shown in Fig. 1. Solid nodes are represented by thick dots on the interface of the fluid domain and no matching is required for the interpolation algorithm.

An adaptation of the Parallel Location and Exchange library (PLE) from Code\_Saturne intended to provide mesh or particle-based code coupling services is employed for the LES-CHT coupling. It allows an easy communication between application codes written in C/C++, Fortran or Python that are running and share the same communicator. This communicator is split so that there is one communicator for the execution of each solver (LES and CHT). The communication between the applications takes place using the intracomunicators created after splitting the global communicator.

### Chemical kinetics and combustion model

The chemistry governing the oxidation of methane is taken into account by the 1-step chemical kinetic mechanism with equivalence ratio correction from Mantel et al. (1996). The Thickened Flame model

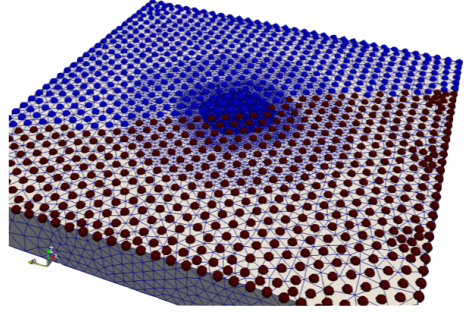


Figure 1: Interface matching between fluid and solid meshes.

from Collin et al. (2000) is employed to thicken the flame front so that it can be resolved in the LES mesh. A dynamic calculation of the local thickening factor  $F$  is employed to correctly compute the flame front in the mesh. The dynamic thickening factor approach from Durand et al. (2005) is followed to obtain the local thickening factor  $F$ :

$$F = 1 + (F_{max} - 1)\Omega \quad (6)$$

where  $\Omega$  is a sensor detecting the presence of the flame front and  $F_{max}$  is the maximum thickening factor allowed in the computation. This sensor can be expressed as a function of a reaction progress  $c$  that is defined as the ratio of mass fraction over stoichiometric mass fraction  $c = 1 - Y_f/Y_{f,st}$ :

$$\Omega(c) = 16(c(1 - c))^2 \quad (7)$$

$F_{max}$  is calculated as:

$$F_{max} = \frac{N\Delta}{\delta_l} \quad (8)$$

where  $N$  is the total number of nodes to reproduce the gradient ( $N=6$  in our current simulation) and  $\delta_l$  is the flame thickness.

### Numerical methods

The LES equations are solved using the Variational Multiscale Stabilization (VMS) technique (Houzeaux and Principe, 2008) by means of the multiphysics code Alya. The discretization of the Navier-Stokes equations yields a coupled algebraic system to be solved at each linearization step within a time loop. Algebraic solvers to solve this coupled problem are not robust enough; the system is therefore split to solve the momentum and continuity equations independently. This is achieved by applying an iterative strategy, namely the Orthomin (1) method for the Schur complement of the pressure (Houzeaux et al., 2011). At each linearization step it is necessary to solve the momentum equation twice and the continuity equation once. The momentum equation is solved using the GMRES or BICGSTAB method (diagonal and Gauss-Seidel preconditioners are usually efficient), and the continuity equation is solved using the Deflated Conjugate

Gradient method (Lhner et al., 2011) together with a linelet preconditioner well-suited for boundary layers. The parallelization of the solver is extensively described elsewhere (Houzeaux et al., 2009). The GMRES solver is also employed to solve for the enthalpy and species mass fractions. The Gauss-Seidel iterative method is employed to solve the species mass fraction until the targeted convergence. The code has been validated in separate efforts (Houzeaux et al., 2009) and no validation results will be shown here for the sake of brevity.

### 3 Computational cases

#### Physical problem

The computational cases considered in this work correspond to a methane premixed flame with stoichiometric equivalence ratio impinging on a flat plate. The nozzle-to-plate distance is  $H/D = 2$  and the inlet velocity is set as 30 m/s using a top-hat velocity profile. The jet inlet diameter is  $D = 0.01$  m and the length of the fluid domain parallel to the plate is  $10H$ . Part of the inlet pipe with length  $H$  is also accounted for in the simulation. The solid part is represented by a squared domain of length  $10H$  and thickness  $H$ . A sketch representing the fluid and solid domains is shown in Fig. 2.

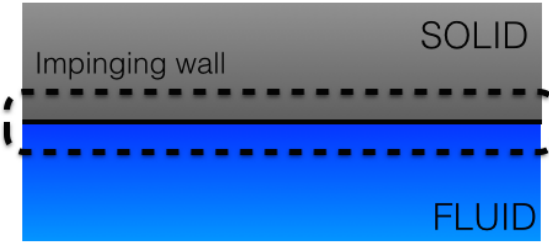


Figure 2: Sketch of the computational domain separating fluid and solid.

The solid domain is treated as a metal body with the thermal and physical properties of copper. In order to keep the synchronization in physical time between the fluid and solid, the metal conductivity was increased by a factor of 100. It means that the solid response to changes in the fluid domain is enhanced allowing to obtain strong variations in temperature across the solid and better visualize the cooling effects on the impinging flame. Real properties of the solid domain are currently being investigated. The boundary conditions in the solid domain are adiabatic conditions on the boundaries and a fixed temperature (Dirichlet-type)  $T_{out}=450K$  on the outer part of the solid domain.

#### Impinging wall treatment

Three different heat transfer conditions at the impinging wall are analysed. Two simplifications that avoid the need of modelling the solid and the entire

coupled problem are compared to the real case where fluid and solid are solved simultaneously. The first case assumes an adiabatic wall, while the second case imposes a Robin condition for the temperature along with the heat flux across the plate. For this approach, the  $T_w$  represents the wall temperature set as 450 K and  $h$  is the convection coefficient set as 50 W/m<sup>2</sup>K. The last case computes the heat flux using the conjugate heat transfer (CHT) approach and imposes a skin temperature on the fluid side, and the heat flux on the solid side (Duchaine et al., 2008).

The boundary conditions specified at the impinging wall (see Fig. 2) for each case are summarised here:

*Adiabatic*

$$-k_f \frac{\partial T}{\partial \vec{n}} = 0 \quad (9)$$

*Robin type*

$$-k_f \frac{\partial T}{\partial \vec{n}} - h(T - T_w) = 0 \quad (10)$$

*Conjugate heat transfer (CHT)*

$$-k_f \frac{\partial T}{\partial \vec{n}} + \nabla \cdot (k_s \nabla T) = \bar{\rho} c_p \frac{\partial T}{\partial t} \quad (11)$$

#### Numerical resolution assessment

The resolution in the fluid domain was assessed by testing three computational meshes of 1.0, 3.5 and 5.2 million elements respectively in cold flow. The results among the three cases were compared for the mean values resulting in similar trends for the last two cases. The maximum normalized wall distance  $y^+$  at the impinging wall was 25, 15 and 10 respectively. As the Reynolds number reduces in reacting flows due to the increase of viscosity inducing an increase of the boundary layer, the mesh with 5.2 million elements was selected to run all the simulations. The resolution of the reacting shear layer was examined by the local thickening factor obtained in the simulations. A maximum local thickening factor of 12 was observed in all the simulations with the finest grid meeting the conditions required by the Thickened Flame model (Collin et al., 2000).

### 4 Results

#### Instantaneous fields

The main flow characteristics of a premixed impinging flame with different type of boundary conditions at the solid wall can be seen in Fig. 3. It shows the three main regions of an impinging flame (Mira et al., 2013): the free jet region, the deflection zone and the development of a wall jet using a scalar representation in the fluid domain. While the adiabatic case shows a distribution of temperature at the level of the cold fuel and combustion products, the cases with heat losses indicate the existence of a thermal boundary

layer where the temperature reduces substantially towards the wall. The temperature for the non-adiabatic cases remains more uniform over the wall and almost a constant value can be observed when the conjugate heat transfer approach is employed. This is related to the fast heat conduction over the solid that cools down the wall. The heat losses influence the formation and convection of the vortex rings as well as the dynamics of the flame in the deflection region. The size of the vortex rings and the convection of these vortices in the radial direction seems to be affected by the heat losses. In addition, the deflection zone is shortened and widened by heat losses affecting the formation of the vortex rings that are less attached to the wall in the adiabatic case. The flow dynamics in Fig. 3 indicates the formation of a wall jet accelerating faster and separating later from the wall for non-adiabatic cases. This will be further examined using the time-averaged flow fields in the next subsection.

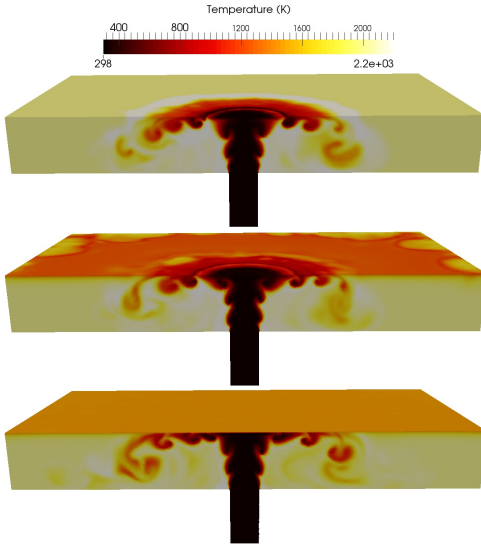


Figure 3: Temperature contour plot for the adiabatic (top), Robin condition (middle) and CHT cases (bottom) at the same time instant  $t = 0.006$  s.

Temperature profiles along the impinging wall also provide fundamental insights into the heat transfer characteristics of the flames under investigation and are shown in Fig. 4. The adiabatic case shows some unphysical overshoots in temperature caused by imposing a zero flux over the boundary with no-slip condition for the velocity. The heat released by the chemical reactions increases the internal energy of the fluid without any dissipation mechanism. Flame/wall interactions take place in this region and the use of adiabatic conditions to account for this phenomenon should be avoided. The plots also show the temperature levels and distribution along the plate where an important reduction in temperature is observed for the cases where heat losses are included. Note that despite the region around the jet centreline is rather similar for all the cases, the temperature profiles away from

this region are quite different. The addition of heat losses in the treatment of solid walls acts flattening the temperature distribution and reducing the temperature variations on the interface. A fast cooling of the solid domain is observed for the case where the conjugate heat transfer is solved that is partially enhanced by the increased conductivity.

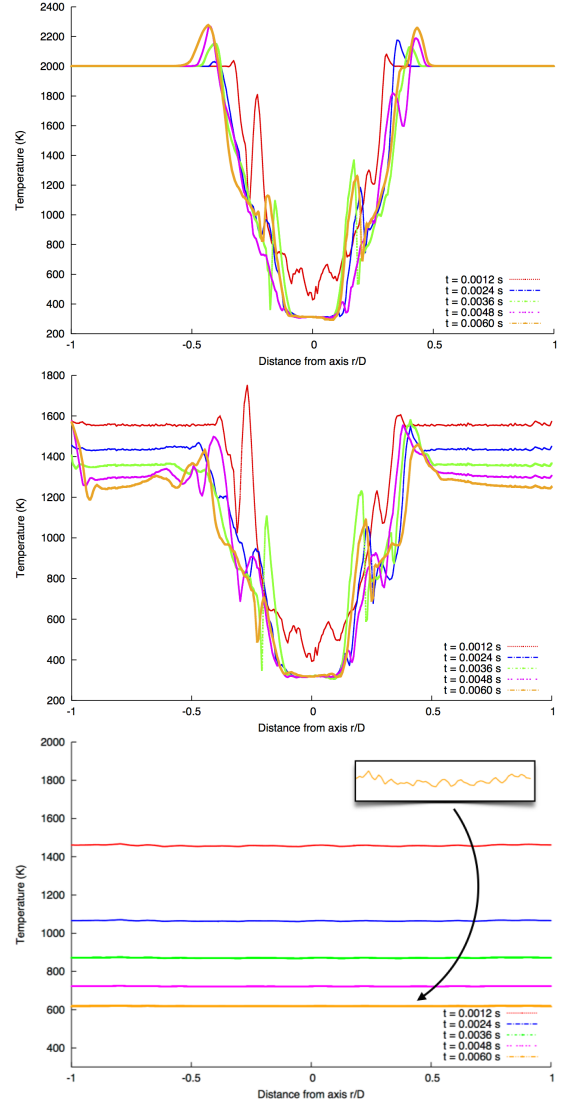


Figure 4: Temperature profiles along the impinging wall for the adiabatic (top), Robin condition (middle) and CHT cases (bottom) respectively.

The mean temperature and heat flux across the impinging plate can be obtained by integrating these variables over the plate surface as follows:

$$\int_{\partial S} (TdS) \quad (12)$$

$$\int_{\partial S} (k \nabla T dS) \quad (13)$$

where  $dS$  represents the differential of area in the outward normal direction to the surface. The time evolution of the plate mean temperature and heat flux pro-

vide information of the cooling characteristics of the different configurations and are presented in Figs. 5 and 6 respectively.

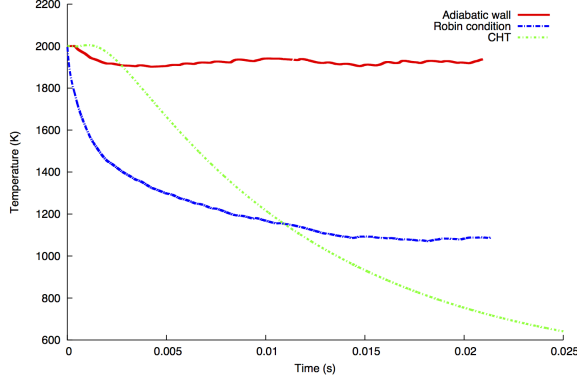


Figure 5: Mean temperature of the impinging plate over time.

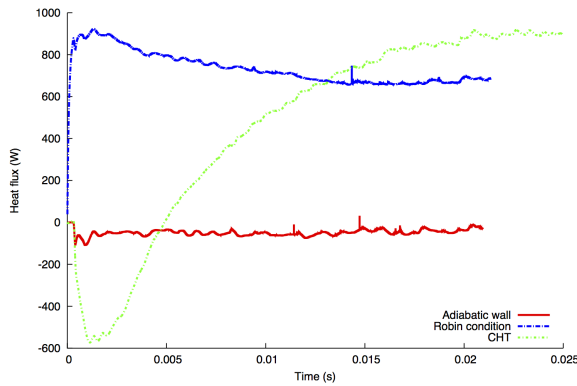


Figure 6: Mean heat flux across the impinging plate over time.

The transient evolution of the temperature and heat flux over the plate shows the response of the solid plate to the flame heating. The wall mean temperature for the adiabatic case shows a negligible variation over time caused by the the condition of zero flux so no heat losses are taken into account. The case with Robin boundary condition shows a decay in temperature respect to the initial condition and converges to a value of around 1150 K. This is the fluid temperature at the start of the thermal boundary layer, since the solid temperature was imposed at 450K. The case with the conjugate heat transfer exhibits the fastest decay in mean temperature over the plate with a mean value around 500K. The response of the solid to the flame heating is achieved by the heat flux across the solid and this is shown in Fig. 6. The case with the CHT is subjected to the largest heat flux and therefore to the lowest skin temperature, which is partially caused by the high conductivity imposed on the solid material. The profiles for the three cases indicate a large heat flux at the start of the simulation caused by the initialization of the domain with hot combustion

products that is eventually reduced to the equilibrium condition as the flame develops. In particular, a heat flux coming from the solid to the flame exists during the initial transient of the simulation that is rather large when the CHT is considered.

The distribution of temperature gradients in the normal direction to the wall over the impinging plate relates the effect of the heat transfer between fluid and solid, and is shown in Fig. 7. A probability distribution of the gradients magnitude over the normalized surface area is also shown as a bottom plot in Fig. 7. It associates the magnitude of the gradients to the portion of area on which they are distributed providing information related to the sensibility of the solid respect to changes in flame temperature. For adiabatic conditions, a zero temperature gradient should be observed. However, regions where the heat release is large at the wall and temperature overshoots appear, a temperature gradient exists to balance the heat equation to satisfy the adiabatic condition. The bottom plot shows that these temperature gradients are rather large and occur at particular locations of the wall. On the other hand, for non-adiabatic conditions, the magnitude of the gradients reduces and extends over a larger part of the surface. This is further examined with the time-averaged fields in the next subsection.

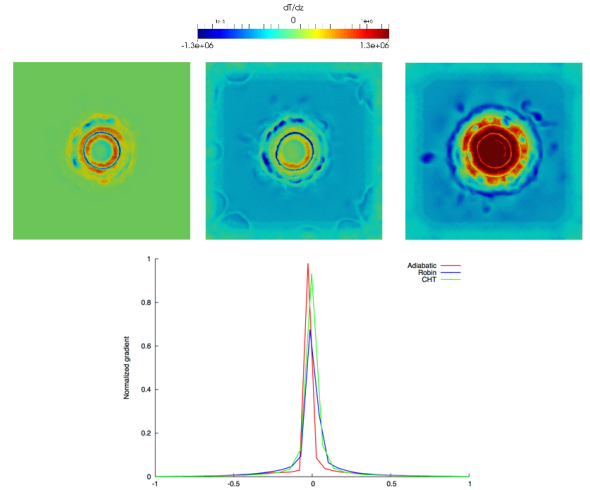


Figure 7: Instantaneous temperature gradient (top) and probability density function of temperature gradients (bottom) at the impinging plate at time  $t = 0.015$  s.

For the CHT case, the distribution of temperature over the fluid and solid domains is shown in Fig. 8 for a given time instant in a streamwise cross section. The core of the flame around the centreline creates a central region of cold temperature on the solid side, while a hot region is found off side the center where the secondary vortices are formed and the combustion heat release interacts with the solid. The heat is distributed across the domain and the temperature distribution along the centreline is shown in Fig. 9. The

temperature rapidly reduces from the impinging wall to the fixed value set on the outer part of the solid domain due to the high conductivity imposed on the solid material.

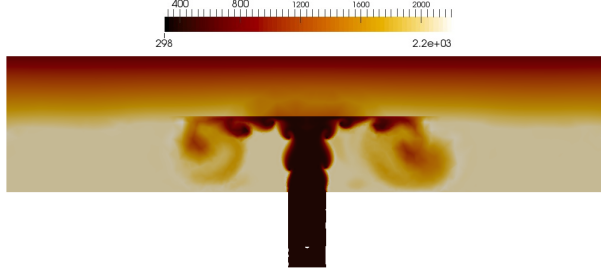


Figure 8: Temperature contour plot for the fluid and solid domains at time  $t = 0.010$  s.

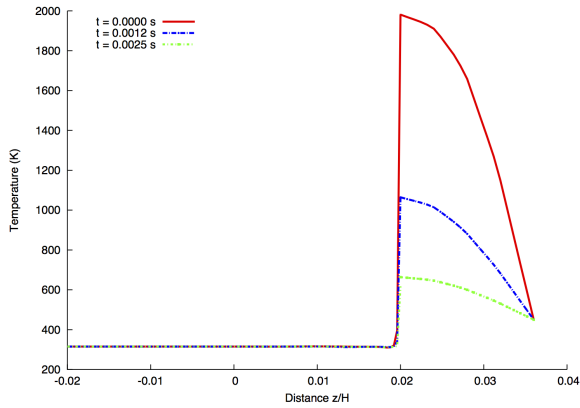


Figure 9: Temperature across the center of the fluid and solid domains at different time instants.

The heat transfer condition also affects the heat release distribution in the near-wall region as seen in Fig. 10. In the free jet region, the heat release rate is rather similar for all the cases, but the differences start appearing in the deflection zone where the vortex rings are formed. The adiabatic condition enhances the chemical reaction rates by sustaining a high temperature region that promotes the release of heat. Figure 10 also shows that the adiabatic case undergoes an enlargement of the reacting region causing the dissimilar temperature distribution observed among the cases. The case with the conjugate heat transfer develops a thin region with chemical reactions taking place changing substantially the heat release distribution.

### Time-averaged fields

The time integration of the instantaneous fields is obtained after time-averaging the data for two flow through calculations using the averaged radial velocity. The time integration is considered after the fields are statistically independent and no effect of the initial conditions exist. The time-averaged fields are employed to investigate the heat transfer effects on the formation of the wall jet and the distribution of tem-

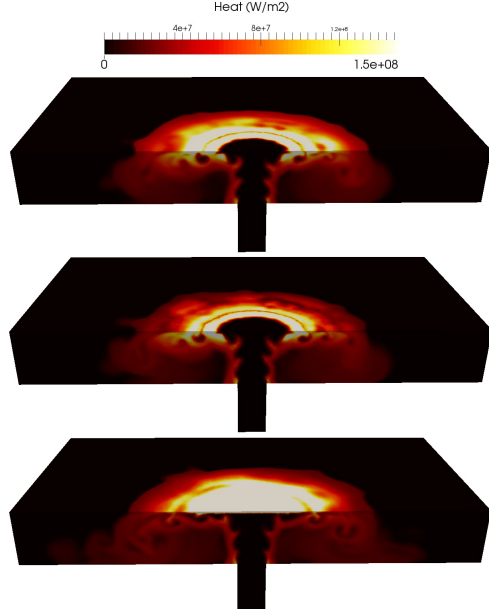


Figure 10: Heat release contour plot for the adiabatic (top), Robin condition (middle) and CHT cases (bottom).

perature gradients.

An important phenomena in impinging flows is the formation of a wall jet. To examine the effects of the wall heat transfer on the formation and development of wall jets, velocity profiles at different radial locations are shown in Fig. 11. Despite the velocity distribution is rather similar among the cases near the centreline, a further acceleration of the flow occurs for the cases with heat losses, specially for the CHT case. The flow with the conjugate heat transfer has the largest peak velocity and the weakest back flow satisfying the conservation of momentum. Results not shown here indicate that the time-averaged shear stresses are the same for all the cases suggesting that the differences in size between the vortex rings are caused by the dissimilar distribution of temperature gradients on the wall. The normalized distribution of temperature gradients on the impinging wall is shown in Fig. 12. The normalization is done with the same values as Fig. 7, so a direct comparison in both magnitude and distribution can be made. Figure 12 evidences the reduction in magnitude of temperature gradients as well as an increase in the area over which the temperature gradients are distributed from the Robin case to the CHT case.

## 5 Conclusions and future work

The study presents some large-eddy simulation results of a premixed impinging jet for a configuration of nozzle-to-plate distance of  $H/D = 2$ . The results presented are focused on the flow behaviour and the heat transfer effects near the impinging plate when different boundary conditions are considered and the conjugate heat transfer is employed on the solid domain. A

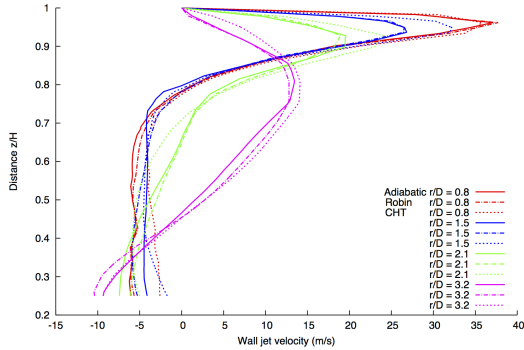


Figure 11: Wall jet development using time-averaged flow fields.

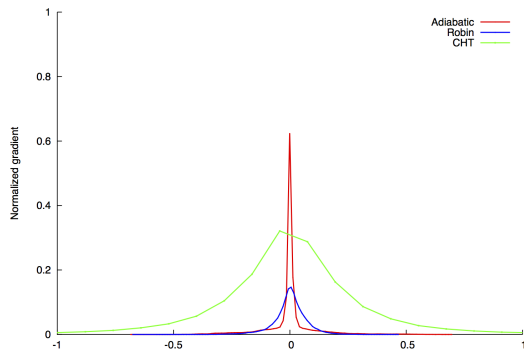


Figure 12: Normalized distribution of mean temperature gradients at the impinging wall.

new coupling algorithm for parallel communication is used to exchange data between the fluid and the solid domain in a efficient manner and without reducing the parallel efficiency of the individual solvers. The results reveal substantial differences when the boundary condition at the impinging wall is changed. Adiabatic conditions lead to a solid wall at high temperature with a large variation in the radial direction, while the non-adiabatic cases show a more uniform temperature distribution over the plate. The effect of heat losses not only tends to reduce the magnitude of the temperature gradients, but also to enlarge the area where the temperature gradients exist. This affects the wall jet development accelerating the flow parallel to the plate and changing the size of the vortex rings, and the dynamics of the flames near the wall. The future work is focused on investigating the properties of the solid domain in the dynamics of the flame and the stability of the coupled problem.

## Acknowledgments

The research leading to these results has received funding through the People Programme (Marie Curie Actions) of the European Union's Seventh Framework Programme (FP7, 2007-2013) under the grant agreement No. FP7-290042 for the project COPA-GT.

## References

Bunker R.S. (2007) Gas turbine heat transfer: Ten remaining hot gas path challenges, *J Turbomach.*, Vol. 129, pp. 193-201.

Colin O., Ducros F., Veynante D. and Poinsot T. (2000), A thickened flame model for large eddy simulations of turbulent premixed combustion, *Phys. Fluids*, Vol. 12, pp. 1843-1863.

Duchaine F., Mendez S., Nicoud F., Corpron A., Moureau V., Poinsot T. (2008), Coupling heat transfer solvers and large eddy simulations for combustion applications, CTR Proc. Summer Program.

Durand L., Huber A., Polifke W. (2005), Implementation and validation of LES models for inhomogeneously premixed turbulent combustion, *Proc. European Combustion Meeting*.

Farhat C. and Lesoinne M. (2000), Two efficient staggered algorithms for the serial and parallel solution of three-dimensional nonlinear transient aeroelastic problems, *Comput. Methods Appl. Mech. Engrg.*, Vol. 182, pp. 499-515.

Fuchs L., Hallqvist T. (2009), Numerical study of impinging jets with heat transfer-inlet conditions effects, AIAA-2009-1578.

Geers L.F.G., Tummers M.J., Hanjalic K. (2004), Experimental investigation of impinging jet arrays, *Exp. Fluids*, Vol. 36, pp. 946-958.

Hadziabdic M. and Hanjalic K. (2008), Vortical structures and heat transfer in a round impinging jet, *J. Fluid Mech.*, Vol. 596, pp. 221-260.

Houzeaux G., Aubry R., Vazquez M. (2011), Extension of fractional step techniques for incompressible flows: the preconditioned Orthomin (1) for the pressure Schur complement, *Comput. Fluids*, Vol. 40, pp. 297313.

Houzeaux G., Vazquez M., Aubry R., Cela J. (2009), A massively parallel fractional step solver for incompressible flows, *J. Comput. Phys.*, Vol. 228, pp. 63166332.

Houzeaux G., Principe J. (2008), A variational subgrid scale model for transient incompressible flows, *IJCFD*, Vol. 22, pp. 135-152.

Jaiman R.K., Jiao X., Geubelle P.H., Loth E. (2006), Conservative load transfer along curved fluidsolid interface with non-matching meshes, *J. Comput. Phys.*, Vol. 218, pp. 372-397.

Lhner R., Mut F., Cebral J., Aubry R., Houzeaux G. (2011), Deflated preconditioned conjugate gradient solvers for the pressure-Poisson equation: extensions and improvements, *Int. J. Numer. Meth. Engrn.*, Vol. 87, pp. 2-14.

Mantel T., Egolfopoulos F.N., Bowman C.T. (1996), A new methodology to determine kinetic parameters for one- and two-step chemical models, CTR Proc. Summer Program.

Mira D., Jiang X., Moulinec C., Emerson D.R. (2013), Numerical investigation of the effects of fuel variability on the dynamics of syngas impinging jet flames, *Fuel*, Vol. 103, pp. 646-662.

Nicoud F., Ducros, F. (1999), Subgrid-scale stress modelling based on the square of the velocity gradient, *Flow, Turb. Combust.*, Vol. 62, pp. 183-200.